AGU PUBLICATIONS

JGR

Journal of Geophysical Research: Solid Earth

RESEARCH ARTICLE
10.1002/2014JB011524

Key Points:
- The 11 March 2011 ($M_w = 9.0$) Tohoku tsunami was recorded by a dense DPG array
- Local phase velocity can be measured based on eikonal tomography
- The prediction of the tsunami wave dispersion is empirically validated

Correspondence to:
F.-C. Lin,
fanchi.lin@utah.edu

Citation:
Lin, F.-C., M. D. Kohler, P. Lynett, A. Ayca, and D. S. Weeraratne (2015), The 11 March 2011 Tohoku tsunami wavefront mapping across offshore Southern California, *J. Geophys. Res. Solid Earth*, *120*, 3350–3362, doi:10.1002/2014JB011524.

Received 7 AUG 2014
Accepted 14 APR 2015
Accepted article online 17 APR 2015
Published online 18 MAY 2015

The 11 March 2011 Tohoku tsunami wavefront mapping across offshore Southern California

Fan-Chi Lin[1], Monica D. Kohler[2], Patrick Lynett[3], Aykut Ayca[3], and Dayanthie S. Weeraratne[4]

[1]Department of Geology and Geophysics, University of Utah, Salt Lake City, Utah, USA, [2]Department of Mechanical and Civil Engineering, California Institute of Technology, Pasadena, California, USA, [3]Department of Civil and Environmental Engineering, University of Southern California, Los Angeles, California, USA, [4]Department of Geological Sciences, California State University, Northridge, Northridge, California, USA

Abstract The 11 March 2011 ($M_w = 9.0$) Tohoku tsunami was recorded by a temporary array of seafloor pressure gauges deployed off the coast of Southern California, demonstrating how dense array data can illustrate and empirically validate predictions of linear tsunami wave propagation characteristics. A noise cross-correlation method was used to first correct for the pressure gauge instrument phase response. Phase and group travel times were then measured for the first arrival in the pressure gauge tsunami waveforms filtered in narrow bands around 30 periods between 200 and 3000 s. For each period, phase velocities were estimated across the pressure gauge array based on the phase travel time gradient using eikonal tomography. Clear correlation was observed between the phase velocity and long-wavelength bathymetry variations where fast and slow velocities occurred for deep and shallow water regions, respectively. In particular, velocity gradients are pronounced at the Patton Escarpment and near island plateaus due to the abrupt bathymetry change. In the deep open ocean area, clear phase velocity dispersion is observed. Comparison with numerically calculated tsunami waveforms validates the approach and provides an independent measure of the finite-frequency effect on phase velocities at long periods.

1. Introduction

In 2011, a dense array of seafloor pressure gauges in the eastern Pacific Ocean off the coast of Southern California recorded the March 2011 ($M_w = 9.0$) Tohoku tsunami with unprecedented spatial and temporal resolutions. By analyzing features in these data, we have the opportunity to gain a better understanding of the physics of tsunami wave propagation and potentially the significance of the elastic compressibility effects on wave velocity [*Tsai et al.*, 2013; *Allgeyer and Cummins*, 2014; *Watada et al.*, 2014]. The ALBACORE (Asthenospheric and Lithospheric Broadband Architecture from the California Offshore Region Experiment) ocean bottom seismometer (OBS) array spanned a region that was 150 km north-south by 400 km east-west, extending into the deep open Pacific Ocean west of the Patton escarpment (Figure 1a) [*Kohler et al.*, 2010, 2011]. In that array, 22 stations with an average spacing of 75 km were equipped with differential pressure gauges (DPGs) that recorded water pressure waveform data continuously at 50 samples per second; DPGs are designed specifically to record low-frequency pressure data with high fidelity [*Cox et al.*, 1984]. The density of the recordings made it possible to observe features in the tsunami waveforms that have never been observed with this level of clarity at this spatial scale.

The ALBACORE DPG tsunami records across the entire array show multiple large-amplitude, coherent phases arriving between 1 h and more than 24 h after the initial tsunami phase (Figure 1b). By contrast, the NOAA Deep-ocean Assessment and Reporting of Tsunamis (DART) buoy system comprises an advanced but much sparser (hundreds of kilometers) array since it is a global, real-time pressure gauge network providing data to constrain the source in tsunami forecasts. The DART system's large station spacing precludes it from producing data with coherent features that provide information about the sources of multiple pulses of high-amplitude energy after the first tsunami wave arrival.

The ALBACORE DPG data were processed by 24-bit data loggers each with an internal clock. GPS time stamps were applied at the beginning and end of the 12 months of deployment, with corrections applied linearly to the data. Most time corrections were under 1 s for the entire 12 month period; the largest was ~4 s for only two stations.

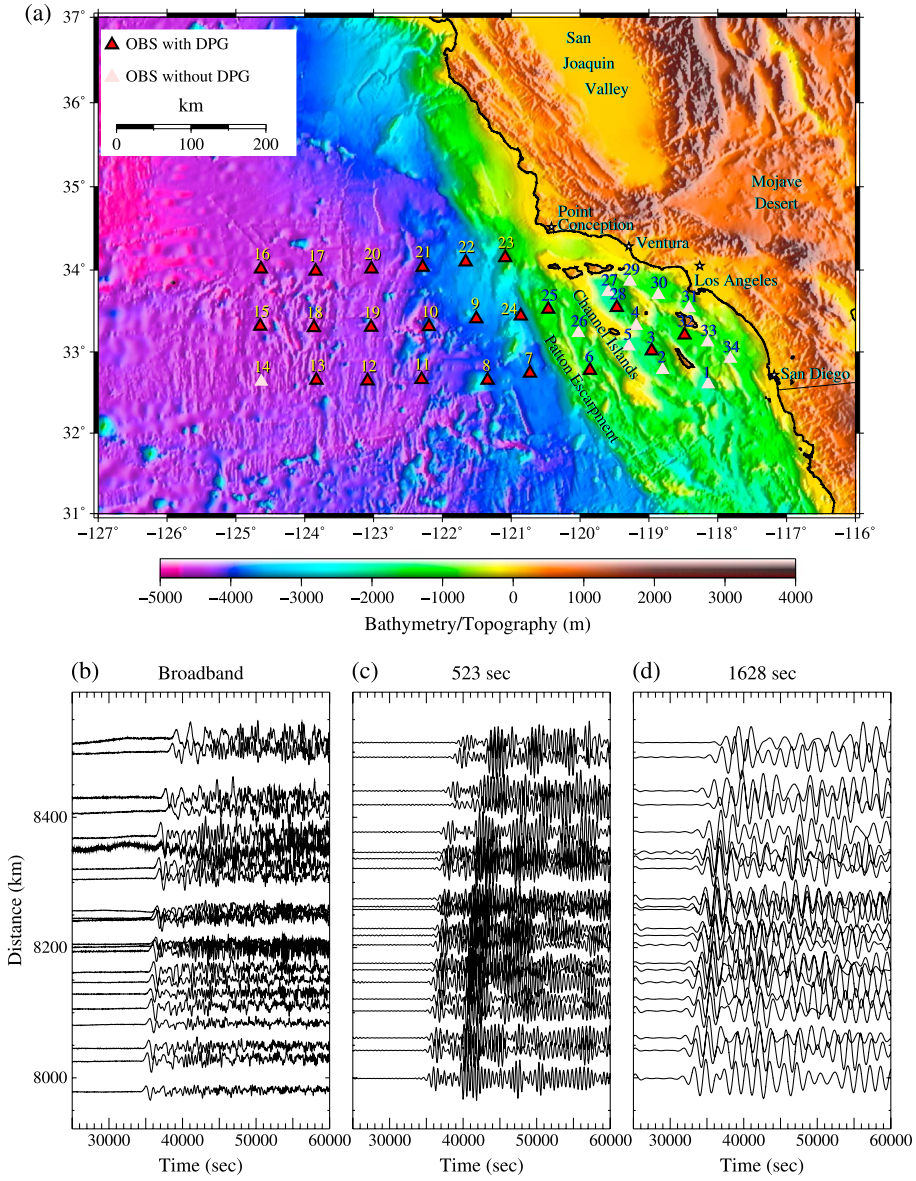

Figure 1. (a) ALBACORE stations with differential pressure gauge (DPG) sensors (red triangles) that recorded the March 2011 Tohoku tsunami. (b) ALBACORE tsunami waveforms recorded on the DPGs shown in Figure 1a. These are pressure wave time series normalized by the same constant to show relative amplitudes. (c and d) DPG tsunami waveforms narrowband filtered around 523 s (middle) and 1628 s (right) are shown. Time is relative to 11 March 2011 $M_w = 9.0$ main shock time.

This is a tsunami wavefront mapping study in which the dense array recordings of the 2011 Tohoku tsunami on the ALBACORE DPG sensors made it possible to track the phase and group travel times and wave velocities across the array. It is rare to have recorded such a large tsunami on a dense array of hydrophones, and this study demonstrates the potential of applying methods primarily designed for earthquake vibration data to low-frequency tsunami waves. The advantage of the dense array data set is that the measurements can be used to validate predictions of phase and group velocities. Specifically, the array data are used to verify the linear, dispersive, gravity-driven ocean wave equation routinely used in tsunami wave simulation between 200 and 3000 s period range. The potential to test whether elastic earth properties can cause small deviations in low-frequency tsunami wave speed [*Tsai et al.*, 2013; *Allgeyer and Cummins*, 2014; *Watada et al.*, 2014] is also discussed.

We first use noise cross-correlation functions to correct for DPG instrument phase response, then use the eikonal tomography approach [*Lin et al.*, 2009] for mapping the Tohoku tsunami wavefront velocity across

the ALBACORE array. Previous to this study, the eikonal tomography method has been applied to earthquake, ambient-noise, and active-source seismic surface waves recorded by dense seismometer arrays to map seismic phase and group velocities [*Lin et al.*, 2011; *Gouédard et al.*, 2012; *Mordret et al.*, 2013; *Lin et al.*, 2013]. The application of the eikonal approach to tsunami data is a natural one because the propagating tsunami wave across the open ocean has characteristics analogous to seismic surface wave propagation. The observed phase velocity dispersion is compared with theoretical and numerical predictions.

2. Theoretical Background

Consider a model that consists of a single fluid layer, with a fixed flat bottom (seafloor with no elastic yielding) and a free upper surface (ocean surface). We then let $H(\mathbf{r}) = h(\mathbf{r}) + \eta(\mathbf{r})$, where H is the total water depth, h is the water depth from a mean horizontal equilibrium surface, η is the tsunami wave height (amplitude) above the equilibrium surface, and $\mathbf{r}$ represents the location on the 2-D surface defined by horizontal coordinates x, y. In the open ocean, h is ~5 km, η is ~5 cm, and wavelength λ is ~0.2 km/s multiplied by the wave period. For the period range we are analyzing, two important ratios need to be considered. The first is that the water depth to wavelength ratio (h/λ) is small (on the order of $<10^{-1}$). This allows us to treat the Tohoku tsunami in open ocean deep water as a horizontally propagating wave with approximately negligible vertical velocity gradients. The second is that the wave amplitude to water depth ratio (η/h) is small (on the order of 10^{-5}) or $h \gg \eta$, which allows us to neglect nonlinearity. Applying these relationships to the Navier-Stokes equations for incompressible fluids leads to the linear, shallow water (continuity and momentum) equations in horizontal coordinates r_i ($i = 1,2$):

$$\frac{\partial}{\partial t}(H) \approx -\sum_i \frac{\partial}{\partial r_i}(hV_i) \tag{1}$$

$$h\frac{\partial}{\partial t}(V_i) \approx -gh\frac{\partial \eta}{\partial r_i} \tag{2}$$

where depth-integrated velocities V_i are found by integration of velocity v_i over vertical coordinate z from the seafloor to the surface:

$$V_i = \frac{1}{H}\int_{-h}^{\eta} v_i \, dz \tag{3}$$

($i = 1,2$) [e.g., *Lin*, 2008]. By taking the time derivative of the continuity equation (1) and subtracting it from the spatial derivative of the momentum equation (2) with the assumption that the still water depth is time invariant, we obtain one form of the wave equation

$$\frac{\partial^2 \eta}{\partial t^2} - \nabla \cdot \left(c^2 \nabla \eta\right) = 0 \tag{4}$$

where c is the phase speed $= (gh)^{0.5}$ and ∇ is the 2-D partial derivative operator [*Lin*, 2008].

If the horizontal gradients in the water depth (bathymetry gradients) are small and smooth such that the gradient of the phase velocity c can be neglected, we obtain a 2-D Helmholtz wave equation that defines low-frequency tsunami wave propagation

$$\frac{\partial^2 \eta}{\partial t^2} = c^2 \nabla^2 \eta \tag{5}$$

[e.g., *Lin*, 2008]. Equation (5) leads to analogies of geometrical optic characteristics that can be made for the ALBACORE observations.

At long periods, where $h \ll \lambda$ and the vertical velocity gradient can be completely neglected, tsunami waves satisfy the shallow water equation, where phase speed $c = \sqrt{gh}$ is nondispersive and depends only on water depth h and gravity g [*Lamb*, 1932]. At intermediate periods, λ is no longer significantly larger then h and the boundary condition consequences of nonzero vertical velocity gradients must be considered. This comprises the shorter-period range examined in this study where the linear, dispersive, water wave equation is governing the tsunami waves. When solutions to equation (5) are represented by simple harmonic

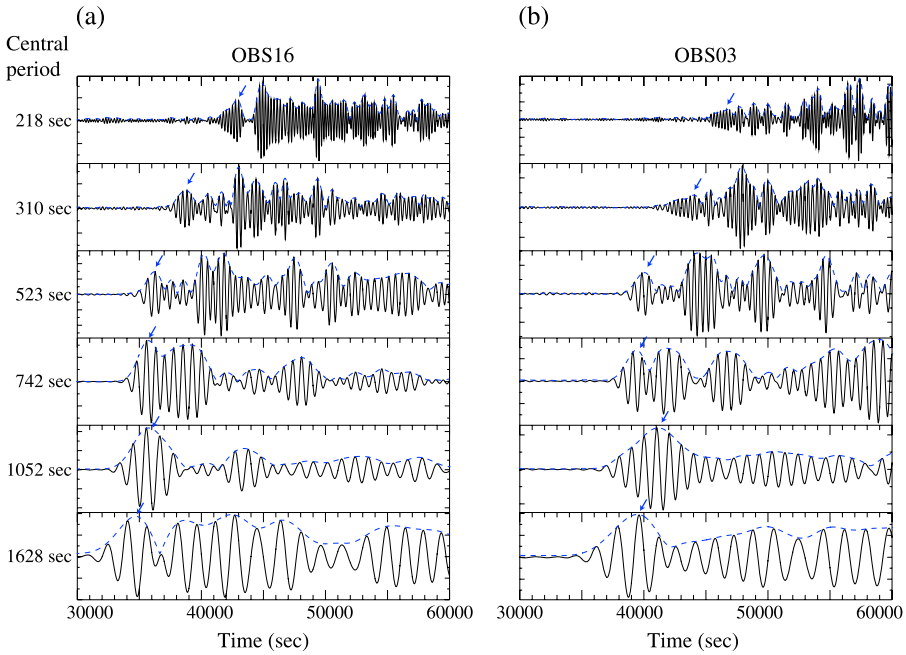

Figure 2. ALBACORE pressure wave time series tsunami waveforms narrowband filtered around six central periods for (a) OBS16 and (b) OBS03. The dashed blue lines denote the envelope functions of the filtered, normalized waveforms. The blue arrow indicates the first group arrival observed at each period.

functions for a range of intermediate wavelengths and water depths (varying h/λ), tsunami wave speeds are defined as

$$c = \omega/k \tag{6a}$$

$$U = \partial\omega/\partial k \tag{6b}$$

$$\omega = \sqrt{gk\ \tanh(kh)} \tag{6c}$$

where c, U, ω, and k are phase velocity, group velocity, angular frequency, and wave number, respectively [*Lamb*, 1932]. The waves display dispersive behavior since wave speed is now also a function of wave number k. The continuum of dispersive behavior is evident in the ALBACORE data with the high-frequency components arriving later than the low-frequency components (Figures 1c and 1d and Figure 2).

Following the derivation for analyzing the properties of seismic surface waves in a 3-D elastic earth [*Wielandt*, 1993; *Lin and Ritzwoller*, 2011], where the effect of lateral velocity variation is assumed to be small, we assume a solution to the (approximate) 2-D wave equation for tsunami waves (equation (5)) that is a function of a harmonic wave with spatially variable amplitude. For each frequency, ω, we model the horizontally propagating tsunami waves as a 2-D wavefield, in which the wave height can be described by

$$\eta(r,t) = A(r)e^{i\omega(t-\tau(\boldsymbol{r}))} \tag{7}$$

where $A(r)$ and $\tau(r)$ are the amplitude and phase travel time, respectively. Substituting this into the wave equation (equation (5)) and equating the real terms of each side yield

$$\frac{1}{c^2(r)} = |\nabla\tau(r)|^2 - \frac{\nabla^2 A(r)}{A(r)\omega^2} \tag{8}$$

which is identical to the elastic earth derivation for 2-D surface waves [*Lin and Ritzwoller*, 2011].

As in seismological studies, it is assumed that the wave amplitude varies smoothly on the single wavelength scale and that the second term on the right-hand side of equation (8) can be neglected. Then, as in the elastic earth example of *Lin and Ritzwoller* [2011], equation (8) reduces to

$$\frac{1}{c(r)} = |\nabla\tau(r)| \tag{9}$$

which is the eikonal equation, a partial differential equation relating the ocean wave travel times to phase velocity distribution. The equation is geometric ray theory in nature where the finite-frequency effects, i.e., the lateral velocity gradients in equation (4) and the amplitude term in equation (8), are neglected [*Landau and Lifshitz*, 1989; *Wielandt*, 1993; *Lay and Wallace*, 1995; *Shearer*, 1999; *Lin et al.*, 2009; *Lin and Ritzwoller*, 2011]. The tsunami waves are finite-frequency in nature, however, where finite-frequency effects due to large lateral bathymetry gradients and wave interference can produce nonnegligible bias on wave velocity estimates based on the eikonal equation (equation (9)).

Ideally, when computing tsunami phase velocities, the contributions from the Laplacian amplitude term (last term in equation (8)) should be calculated using wave amplitude measurements to mitigate biases due to wave interference. However, in the case of ALBACORE, the DPG sensor distribution is not dense enough to calculate a second-order spatial derivative term empirically across the array. To evaluate the potential bias introduced by ignoring the amplitude term in equation (8) when estimating phase velocities based on the eikonal equation (equation (9)), we also apply eikonal tomography to numerically simulated tsunami waveforms. We simulate the Tohoku tsunami at the ALBACORE station locations by solving the nondispersive, shallow water, gravity-driven ocean wave equations using ETOPO1 bathymetry [*Amante and Eakins*, 2009]. Our calculations use a multigrid, coupled tsunami model (Cornell Multi-grid Coupled Tsunami Model) with the linear solver [*Liu et al.*, 1998]. The bottom friction terms in the momentum equations are represented by Manning's formulation, which contains the Manning relative roughness coefficient, since the algorithm is meant for both shallow and deepwater application. For our open ocean deepwater locations, friction effects on the propagating tsunami are negligible. Coriolis force is included in the simulation. The finite-fault model of *Shao et al.* [2011], based on inversion of long-period body and surface waves, is used for source representation in the forward calculations.

In section 3.2, we describe how the eikonal tomography approach is applied to both the observations (ALBACORE DPG data) and to the numerically calculated (synthetic) waveforms. Comparisons of phase velocity dispersion in the data to synthetic waveforms are used to evaluate the finite-frequency effects and other effects that are not accounted for in the nondispersive, shallow-water approximation. Based on the synthetic waveforms, we also test how the presence of a hypothetical dense array can be used to better account for finite-frequency effects by solving the complete Helmholtz equation (equation (8)). We note that the effect of bathymetry gradient is accounted for in our nondispersion shallow-water numerical synthetics. Constraining the effect of bathymetry gradient in real observations, however, requires recordings of waves propagating in different directions. As we are only analyzing the first arrival of the Tohoku tsunami wavefront here, developing a method to evaluate the effect of large bathymetry gradients is out of the scope of this study.

3. Method and Results

3.1. Differential Pressure Gauge Phase Correction

Prior to measuring the travel times and velocities, we used a noise cross-correlation method to make an instrument phase correction to the observed tsunami waveforms. The different instrument phase responses among different DPGs, which can vary as a function of period, have been observed on other recently recorded data sets (Don Forsyth and Spahr Webb, personal communication). While its source is not understood, one possibility is that the capillary tube that is the conduit for the exchange of oil between the inner and the outer chambers inside the DPG becomes clogged, impeding the consistent flow of oil between the two chambers (Timothy Kane, personal communication). Regardless of cause, noise cross-correlation methods can be used to estimate the phase shift between two DPGs in order to make a correction to tsunami wave travel times [e.g., *Stehly et al.*, 2007].

To obtain the phase shift corrections for the DPG sensors, we calculate the cross-correlation functions between every pair of DPG sensors for 1 year (2010–2011) of ambient vibration data. Assuming a diffusive noise wavefield, cross-correlation signals in both positive and negative time lags are expected to be identical and can be related to the Green's function between the two locations [*Bensen et al.*, 2007]. By examining the asymmetry of noise cross correlations, relative phase travel time shift between each station in a pair can be evaluated [e.g., *Stehly et al.*, 2007]. Similar to seismic ambient noise cross correlations with

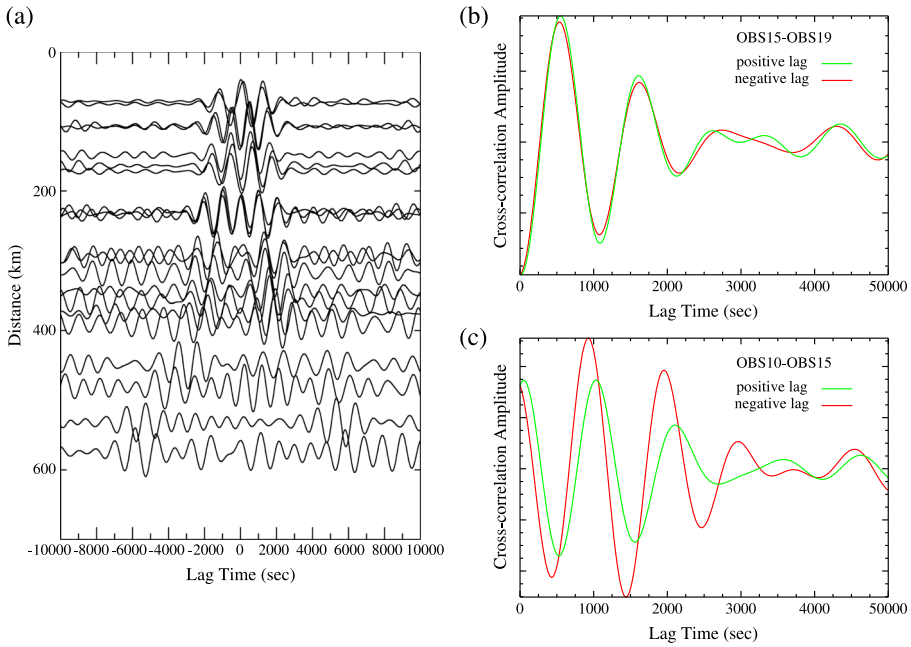

Figure 3. (a) Noise cross-correlation functions between OBS15 and all other DPG locations (see Figure 1a for station locations) for 1 year of waveform data. Clear gravity ocean wave signals can be observed. (b) Comparison of positive and negative component noise cross-correlation function between OBS15 and OBS19 showing no relative time shift. (c) Same as Figure 3b but for station pair OBS10 and OBS15 where a clear relative time shift is observed.

good noise source distribution, good signals are observed in both negative and positive times for the majority of the DPG cross correlations (Figure 3a). For cases where the noise correlation functions are mostly symmetric about the zero time axis (i.e., no relative time lags; e.g., Figure 3b), we conclude that the time shift error between the two DPGs, if it exists, is insignificantly small. For cases where there is a clear relative time shift between positive and negative times (e.g., Figure 3c), a timing correction is needed to account for the time shift error between the two stations. We estimate the period-dependent phase time shift error between each station pair by cross correlating the positive component with the negative component of the noise correlation function for lag times between 0 and 5000 s. We discard all measurements with signal-to-noise ratio (SNR) smaller than 3.

To determine the phase time shift error for a particular station, we first define 10 stations (OBS08, OBS09, OBS11, OBS15, OBS17, OBS18, OBS19, OBS20, OBS21, and OBS22) as the reference stations. These stations are defined as reference stations because no systematic relative phase time shift is observed between them for 200 s to 2000 s periods (e.g., Figures 4a and 4b). Note that the signals in noise correlation functions are clearest for periods between 200 and 1200 s, and the estimated time shift errors are more scattered for periods longer than 1200 s due to the poorer signal quality. Figures 4c and 4d show two examples of DPG stations (OBS10 and OBS12) with clear time shift errors relative to the 10 reference stations. The time shift error, in general, increases with period, and the time shift error can be larger than 100 s at long periods (OBS12; Figure 4d).

For each station, we estimated the period-dependent travel time correction by fitting a linear function to the computed time shifts for periods smaller than 1200 s and we use a flat line for periods longer than 1200 s. There is strong scattering at periods longer than 1200 s due to the degrading noise correlation function signal quality. Moreover, there is some indication that the timing error flattens out for periods longer than 1200 s perhaps due to saturation in DPG time shifts at these long periods [*Cox et al.*, 1984] (Figures 4c and 4d). To avoid overcorrection, we simply assume a flat line with zero slope for the fits above 1200 s. Table 1 documents the best fitting slope and intercept for all stations' time shifts for periods smaller than 1200 s. As we will show, these instrument phase corrections are essential to obtaining accurate phase velocity measurements based on eikonal tomography.

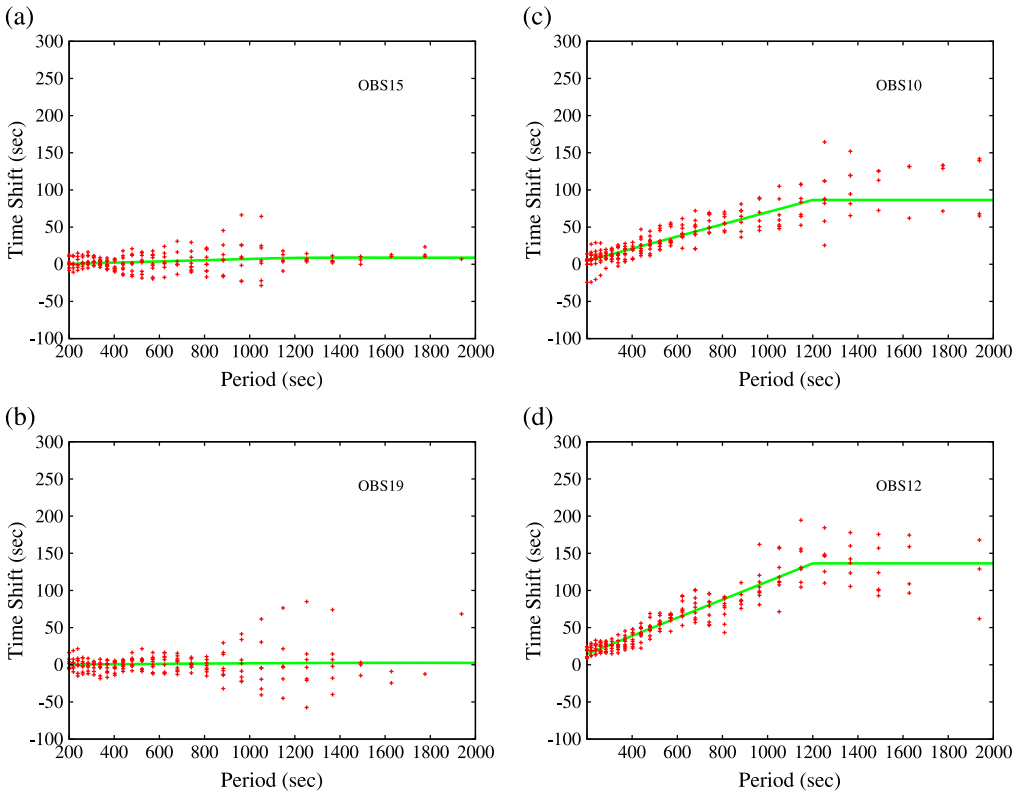

Figure 4. Estimated time shifts between four example stations and the 10 reference stations as a function of period. Results for (a) OBS15 showing no relative time shifts for the entire period range, (b) OBS19 showing no relative time shifts, (c) OBS10 showing an increase in time shift as a function of period, and (d) OBS12 showing an increase in time shifts. Results exceeding a predefined SNR level are shown; fewer long-period estimates exceed an acceptable SNR limit. The solid green lines indicate the best fitting time-shift correcting curves.

Table 1. Best-fitting Slope and Intercept for All Stations' Time Shifts for Periods Smaller Than 1200 s

Station	Slope (s/s)	Intercept (s)
OBS03	0.039442	−12.444
OBS06	0.0244001	−4.22975
OBS07	0.0410225	−8.84208
OBS08	−0.0234612	8.52332
OBS09	0.00821712	−2.06501
OBS10	0.081856	−11.7439
OBS11	−0.011585	4.78537
OBS12	0.121873	−9.86253
OBS13	0.0997306	−15.6966
OBS15	0.00841514	−1.23488
OBS16	0.0432894	−3.31881
OBS17	0.012762	−4.10009
OBS18	0.00285076	−0.897218
OBS19	0.00230907	−0.887863
OBS20	−0.00208501	−0.87893
OBS21	0.0170498	−5.19884
OBS22	−0.0144053	1.94666
OBS23	0.0276171	−5.40799
OBS24	0.026491	−9.15055
OBS25	0.132282	5.37368
OBS28	0.0568756	−10.4655
OBS32	0.07961	−35.0462

3.2. Travel Times and Eikonal Tomography

We modify the traditional frequency-time analysis for seismic surface waves [*Bensen et al.*, 2007] to measure the tsunami wave first-arrival group and phase travel times for both observed and synthetic waveforms. For each station, a series of 30 Gaussian filters with center periods ranging from 200 to 3000 s and sigma (half-width) equal to 4.5% of the central period is applied to obtain the band-pass-filtered tsunami waveforms (e.g., Figure 2). For each period, we calculate the envelope and phase functions of the filtered waveform using the Hilbert transform [*Levshin et al.*, 1989]. All local maxima of each envelope function within the predicted time window associated with velocities from 0.1 to 0.4 km/s are considered

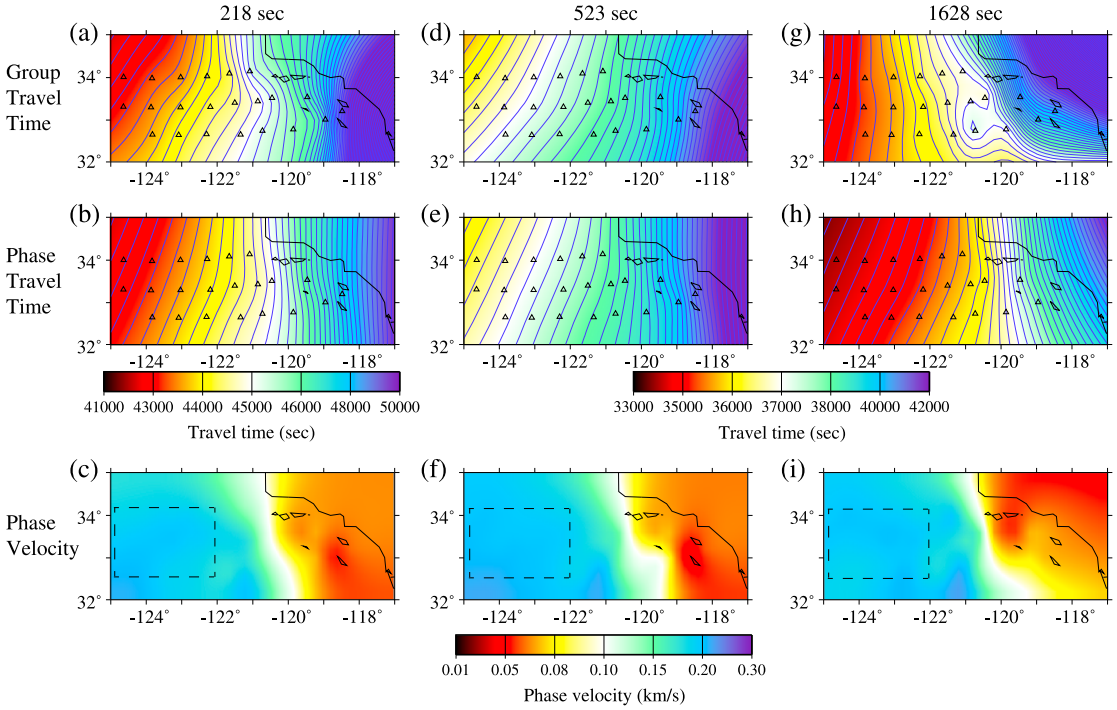

Figure 5. (a–c) Group travel time, phase travel time, and phase velocity maps for 218 s period from the DPG data. The travel time contours are separated by 200 s. The dashed box in Figure 5c indicates the open ocean region used in Figure 7. (d–i) Same as Figures 5a–5c but for 523 s and 1628 s periods, respectively.

first group arrival candidates. For station OBS16, which is in the open ocean and has a clean tsunami waveform (Figures 1a and 2a), the first group arrival for each period is determined by the first local maximum with amplitude higher than 8 times that of the noise level. For each period, we define the noise level as the average amplitude of all local maxima arriving between 20,000 and 30,000 s after the tsunami source earthquake, corresponding to 1–4 h before the first arrival at the ALBACORE array.

With the first group arrival at OBS16 determined (Figure 2a), we then consecutively track the first group arrival at all other stations. To determine the first group arrival for a target station, the already determined group arrival time from the nearest station is used to estimate the overall group velocity of the tsunami wave propagating across the entire Pacific Ocean (the great circle distance divided by the group travel time). The estimated group velocity is then used to predict the group arrival time for the target station where the closest group arrival candidate is then chosen as the first arrival. With all the first group arrival times determined, a minimum curvature surface fitting [*Smith and Wessel*, 1990] is applied to interpolate travel time measurements onto a 0.2°× 0.2° regular grid to construct the group travel-time maps (e.g., Figures 5a, 5d, and 5g).

We determine the phase travel time based on the phase measured at the first group arrival time [*Lin et al.*, 2008]. Note that a relatively accurate reference phase velocity and source mechanism is needed to resolve the 2π ambiguity and determine the exact phase travel time. It is, however, possible to resolve the relative phase information based on phase-front tracking without the exact knowledge of a reference phase velocity [*Lin and Ritzwoller*, 2011]. Here similar to the group travel time approach, we first determine the phase travel time at station OBS16 and then consecutively determine the phase travel time for all other stations. We approximate the group velocity determined at OBS16 as the reference phase velocity and predict the phase travel time for OBS16. With the predicted travel time, the 2π ambiguity can be resolved, and we can determine the phase travel time based on the phase measurement [*Lin et al.*, 2008]. The phase travel time determined at OBS16 is used as the starting point to consecutively resolve the 2π ambiguity and determine the phase travel time at the other stations. To determine the phase travel time at a target station, the average phase speed for the nearest corrected station (the great circle distance divided by the phase travel time) is used as the reference. We apply the instrument phase travel time corrections

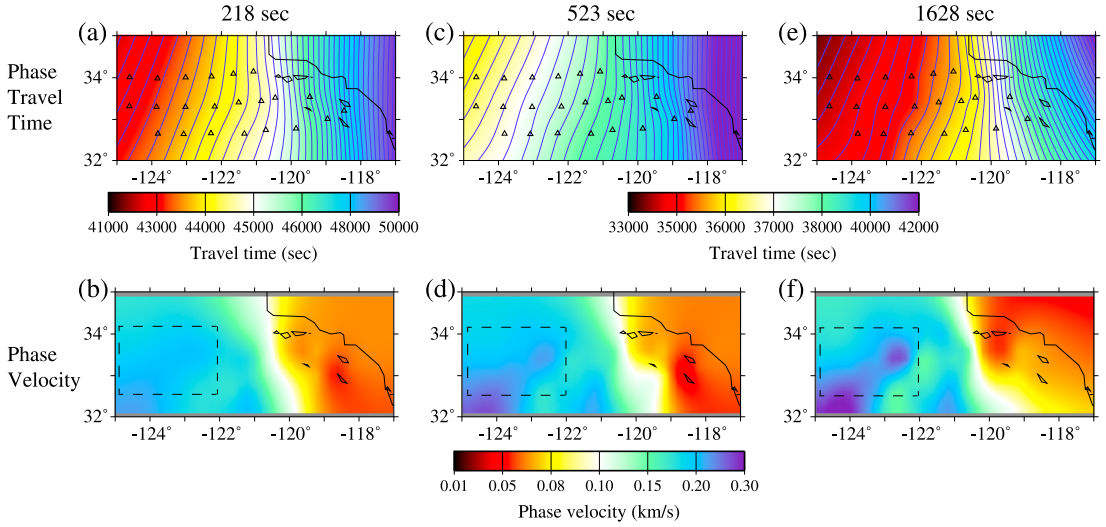

Figure 6. Same as Figures 5b, 5c, 5e, 5f, 5h, and 5i but without time shift corrections.

estimated by noise cross-correlation functions (section 3.1) to reduce travel time errors. After all phase travel times are determined, similar to group travel time, a minimum curvature surface fitting is applied to construct the phase travel-time maps (e.g., Figures 5b, 5e, and 5h). While the absolute phase travel times can be biased by the uncertainties in source mechanism and the approximation of group velocity as phase velocity for OBS16, the relative travel time information between stations should be accurate.

Examples of the 218 s, 522 s, and 1628 s period 2011 Tohoku tsunami wave group and phase travel time maps recorded by the ALBACORE DPG array are shown in Figure 5. Overall, travel time increases as the wave approaches the California coastline as expected. Complications are present near the Patton Escarpment particularly for group travel time measurements at long periods for the ALBACORE DPG data (Figure 5g). This is likely due to interference of the direct and reflected waves, which not only results in a small-scale group travel time anomaly for station OBS07 but also changes the overall apparent group propagation direction. Phase travel time measurements are, in general, more stable than group travel time measurements, and we will focus on deriving phase velocities based on the phase travel time measurements.

Following the eikonal tomography method described in *Lin et al.* [2009], for each period, we determine the phase velocity at each location by the gradient of the phase travel-time map based on the eikonal equation (equation (9)). The phase velocity maps for 218 s, 523 s, and 1628 s periods for the ALBACORE DPG data are shown in Figures 5c, 5f, and 5i as examples. Clear correlation between the phase velocity and bathymetry is observed, where fast and slow velocities are observed for deep and shallow water ocean areas, respectively (Figure 1a and Figures 5c, 5f, and 5i). In particular, velocity gradients are pronounced at the Patton Escarpment and near island plateaus, likely due to the abrupt bathymetry change. Note that only the phase velocities within areas with good station coverage are considered meaningful.

It is essential to correct for the instrument phase time shift between stations within the open ocean area before applying eikonal tomography to estimate the phase velocities particularly at long periods. Figure 6 shows the phase travel time measurements and estimated tsunami wave velocities if no time correction is applied. Clear, small-scale, wavefront distortion and velocity anomalies that are not correlated with the bathymetry (Figure 1a) are observed at long periods within the open ocean. Based on the time shift errors estimated by noise cross-correlation functions (Table 1), we determine that timing corrections are particularly needed for four DPG stations (OBS10, OBS12, OBS13, and OBS16) in the open ocean area. After applying the timing correction for the four stations (based on Table 1), the small-scale wavefront distortion and velocity anomalies in the open ocean are mostly removed as shown in Figure 5. Note that the corrections do not necessarily give us correct absolute phase times, but this is not necessary for our application. Because we are measuring relative travel times for the phase velocity analysis, the final solutions are correct as long as the times for all stations are consistent with each other. Since our phase velocity analysis is based on relative travel times, a constant phase shift (i.e., if all stations are shifted by the same amount) will not affect our result.

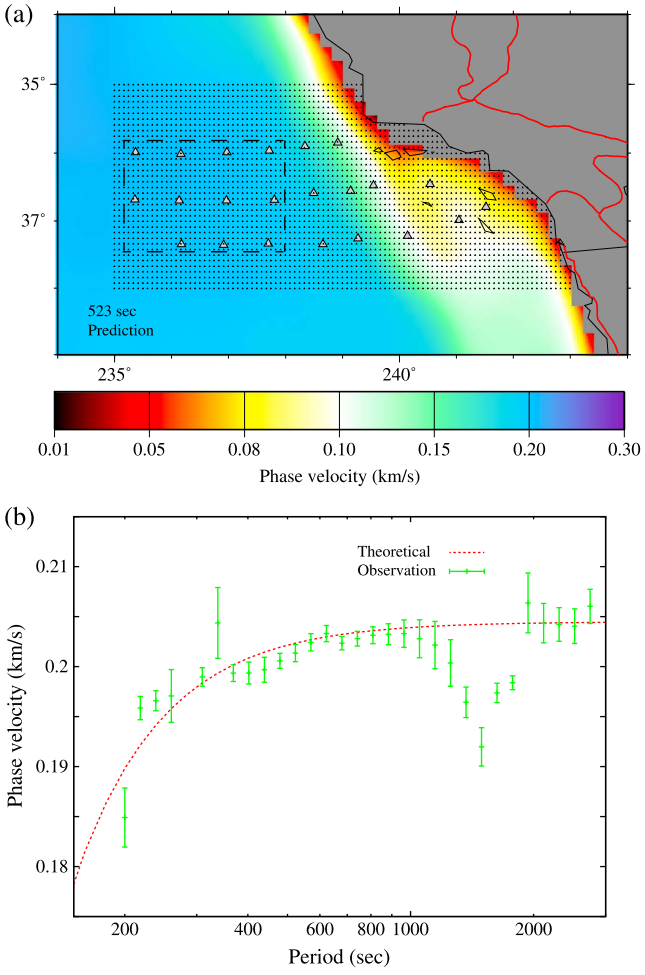

Figure 7. (a) The predicted phase velocity map for 523 s based on the ETOPO2 bathymetry model, gravitational acceleration $g = 9.8$ m/s, and equation (6). Note that we remove small-scale bathymetry features using a 0.3° Gaussian filter before the calculation of the prediction. The dashed box indicates the open ocean region used to calculate the predicted and observed average phase velocity. The dense grid shows the hypothetical dense array used in the synthetic test. (b) Averaged phase velocity dispersion curves calculated for ALBACORE observations (solid green bar symbols) and predicted (dashed red curve) values within the open ocean region in Figure 7a. The vertical lines for observed calculations indicate standard deviations from the mean; lengths can be determined from the *y* axis.

4. Discussion

The ability to track a tsunami wave and determine phase velocity variation across a dense array allows the linear dispersive water wave equation (equation (6)) to be validated locally and empirically for the first time. Here we focus our analysis on the open ocean area (defined in Figure 7a) where the tsunami waveforms are simpler and the bathymetry variation is small. In the area selected (Figure 7a), the predicted phase velocities based on the ETOPO2 bathymetry model [National Geophysical Data Center, 2006] (smoothed using a 0.3° Gaussian filter) are mostly constant at each period, and we can compare the observed and theoretically predicted (using equation 6) averaged phase velocities (Figure 7b). We determine the uncertainty of the observed average phase velocity (i.e., standard deviation of the mean) based on one fifth of the standard deviation of the velocity variation within the entire open ocean area. The one fifth comes from the fact that there are approximately five areas with independent constraints on velocities (five square areas with stations on all four corners) despite the fact that the errors in the velocity measurements are not independent (if one area is fast, the areas adjacent to it are more likely slow). Hence, the variability of the velocity measurements should be evenly divided by the number of constraints when estimating the uncertainty of the average.

The observed average phase velocity dispersion in the open ocean area is, in general, consistent with the prediction based on the linear dispersive water wave equation (equation 6) (Figure 7b). Similar to the prediction, the observed phase velocities (besides the velocity reduction near 1500 s) are mostly flat above 600 s period, where $c = \sqrt{gh}$ for the ideal, shallow-water case explains the observations. At shorter periods (<600 s), the observed phase velocities decrease gradually with a decrease in period to where ~10% velocity reduction is observed at 200 s period compared to the nondispersive velocity at long period. In this intermediate-period range, where a single wavelength is no longer significantly larger than the water depth, the nonzero vertical velocity gradients of the water wave cannot be completely neglected and the dispersion of the phase velocity (equation (6c)) must be considered to explain the observation.

Above 1000 s period, the tsunami wave reflected off the steep bathymetry contrast across the Patton Escarpment is likely interfering with the first arrival and affecting our ability to make accurate travel time

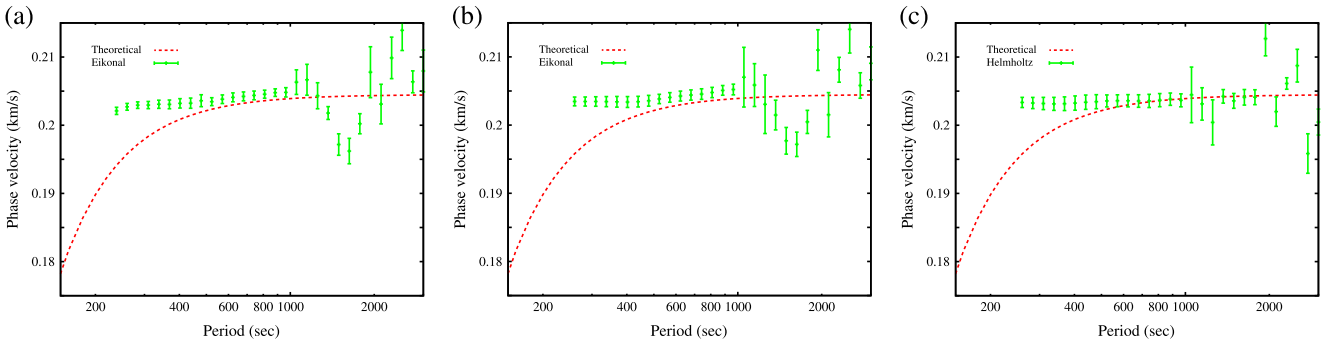

Figure 8. (a) Same as Figure 7b but for the synthetic waveforms at the DPG station locations. The average phase velocities and their uncertainties determined using eikonal tomography are shown as the solid green bar symbols. The theoretical phase velocity dispersion curve based on equation 6 is indicated by the dashed red line. (b) Same as Figure 8a but with the synthetic waveforms from a hypothetical dense array (Figure 7a). (c) Same as Figure 8b but the phase velocities are determined using the full solution to the Helmholtz equation (equation (8)).

and phase velocity measurements (Figure 5g). To assess the validity of the eikonal tomography approach at long periods and understand whether the velocity reduction near 1500 s period is due to finite-frequency effects, we apply the same eikonal methodology to the synthetic waveforms at the DPG station locations to calculate phase velocities. We also perform eikonal tomography and Helmholtz tomography with synthetic waveforms on a hypothetical dense array with stations distributed evenly on a regular 9 km × 9 km grid (Figure 7a). This allows us to evaluate the finite-frequency effect due to wave interference that can be accounted for by the amplitude term in equation (8). Since no dispersion is expected in the numerical waveforms, determining the time of the first arrival at each station is achieved by finding the maximum waveform amplitude near a reference time that is approximately the same for all periods. Due to the extremely low amplitude of the first arrival near 200 s period, we cannot confidently pick the first arrival from the synthetic waveforms; hence, we did not analyze the result at the two shortest periods. For all other periods, we apply the eikonal and Helmholtz tomography methods to the synthetic phase travel times and amplitudes and obtain analogous phase velocity maps (not shown here). We then calculate the average phase velocities over the same open ocean area (Figure 7a) to obtain the average velocities and their associated uncertainties for the synthetic waveforms.

Figure 8a shows the results of applying the eikonal approach to the synthetic waveforms at the DPG station locations and averaging the velocities over the open ocean area. For intermediate periods (500 to 1000 s), the average phase velocities, while slightly overestimated, follow the theoretical values closely. For short periods ($<$500 s) the phase velocities deviate from the theoretical values but remain approximately constant due to the nondispersive nature of the synthetic waveforms. Velocity discrepancies at long periods ($>$1000 s), on the other hand, likely result from eikonal tomography methodology errors. Above 1000 s period, the open ocean area we selected is within one wavelength (~200 km) of the Patton Escarpment and the finite-frequency effect due to the interference of the direct with reflected wave is likely important.

We use the synthetic waveforms across a hypothetical dense array (Figure 7a) to show the exact finite-frequency effect of wave interference and how the amplitude term in the solution of the Helmholtz equation (equation (8)) can be used to account for it. Figures 8b and 8c show the average phase velocities observed across the open ocean area based on the solution of the eikonal (equation (9)) and Helmholtz solution equations (equation (8)), respectively. Here in contrast to the sparse DPG station distribution, the hypothetical dense array allows the second derivative of the first arrival wave amplitude to be determined. Overall, the average phase velocities observed using eikonal tomography (Figure 8b) are very similar to that determined by the sparse synthetic waveforms (Figure 8a), suggesting that the average velocities observed using eikonal tomography is not sensitive to station density. The average phase velocities based on the Helmholtz tomography (Figure 8c), on the other hand, better match the theoretical predictions between 1000 s and 2000 s period and are generally nondispersive across the entire period range, consistent with the numerical input. This confirms that the observed velocity dip near 1500 s resulting from eikonal tomography (Figure 7b and Figures 8a and 8b) is due to finite-frequency effects that can be accounted for using the full solution to the Helmholtz equation. Above 2000 s, large errors are present,

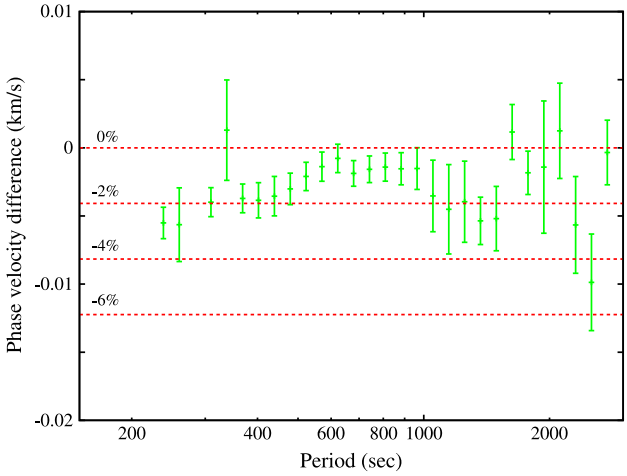

Figure 9. Residual phase velocities and their uncertainties determined from the difference between the observed (Figure 7b) and synthetic (Figure 8a) phase velocity dispersion curves (solid green bar symbols). The uncertainties are estimated based on the root-mean-square of the uncertainties in Figure 7b and Figure 8a; size of error bar can be obtained from the vertical axis. The dashed red lines indicate percentage velocity deviation from nondispersive theoretical phase velocity calculation based on $c = \sqrt{gh}$.

likely due to severe wave interference. In this case, the first arrival is not always well defined since the entire study area is roughly within one wavelength distance of the Patton Escarpment.

Assuming velocities estimated from both data and synthetic waveforms (Figures 7b and 8a) suffer from the same bias introduced by eikonal tomography (e.g., the dipping feature near 1500 s period in Figures 7b and 8a likely related to the finite-frequency effect due to wave interference), the velocity difference between the two should remove that bias. This residual (Figure 9) is then due to other physical effects that are not included or properly accounted for in the numerical simulation. Note that the uncertainties shown in Figure 9 are based on the root-mean-square of the uncertainties estimated for both the observed and synthetic average velocity results. The difference at short periods (<600 s) as shown in Figure 9 is due primarily to the nondispersive effects in the shallow-water approximation. Between 600 and 2000 s, the observed phase velocities based on the observations tend to be slower than those based on numerical simulation. This may be due to the elastic property of the solid earth [*Tsai et al*., 2013; *Allgeyer and Cummins*, 2014; *Watada et al*., 2014] or other effects that are not accounted for when using the shallow-water equation to simulate the tsunami wavefield. Caution must be taken when interpreting the long-period result as it is also unclear whether the finite-frequency bias is identical in data and synthetic waveforms. Due to the significant bathymetry variation near the Patton Escarpment, the synthetic tsunami can easily overestimate or underestimate the reflected tsunami wave and introduce discrepancies between the synthetic and observed measurements. As we demonstrate with the synthetics, a denser pressure gauge array with similar observations would allow the Laplacian of amplitude to be calculated and can potentially resolve this problem.

A theoretical study by *Tsai et al*. [2013] suggests that the elastic deformation of the solid earth can potentially reduce the tsunami wave speed at long periods (~0.2% at 1000 s period and ~1% at 5000 s period) computed for a homogeneous elastic half space without an inertia term. *Watada et al*. [2014] show reductions of 1% at 1000 s and 1.5% at 5000 s based on normal mode theory for a preliminary reference Earth model that includes the effects of the inertial term, elastic solid earth, compressible seawater, and geopotential change. In such a case, the seafloor is no longer assumed to be rigid and an additional perturbation term is introduced when deriving the 2-D water wave equation. Our results support the hypothesis that elastic deformation effects may reduce the phase velocities at long periods (Figure 9), but the uncertainties also prevent us from concluding that all errors or other effects are fully accounted for.

5. Conclusions

The deployment of the dense ALBACORE DPG array offshore Southern California captured the tsunami wave produced by the 11 March 2011 ($M_w = 9.0$) Tohoku earthquake and provides a unique opportunity to study tsunami wave propagation. Similar to seismic surface-wave phase velocities, which depend on subsurface earth structure, the tsunami wave can be considered a 2-D wave propagation phenomenon where local velocities are primarily dependent on water depth, with a much smaller dependence on variations in water density due to salinity and temperature. We first demonstrate that DPG noise cross correlations can be used to calibrate DPG instrument phase response. We then demonstrate the potential of using the

eikonal tomography approach for mapping tsunami wavefronts and determine phase velocities across the dense pressure gauge network. In order to evaluate the finite-frequency effect due to wave interference, which can be accounted for using Helmholtz wave equation analysis, we compute numerical tsunami waves at the ALBACORE station locations. We examine the differences in average phase velocities between observed and synthetic data at long periods to quantify the finite-frequency effect as a function of tsunami wave frequency.

The derived 2-D tsunami phase velocity maps across the ALBACORE array show clear correlations between observed velocities and water depth. We show that the observations in the open ocean region can be used to validate phase velocity dispersion predictions based on the linear dispersive water wave equation. The higher uncertainties at long periods preclude us from coming to an unequivocal conclusion about the elastic earth effect on tsunami wave propagation. Better understanding of the absolute amplitude measurements in data, along with even denser arrays, can reduce the uncertainties by accounting for finite-frequency effects.

Acknowledgments

The tsunami waveform data from the ALBACORE DPG array are available at IRIS Data Management Center. The IRIS Data Management System is funded through the National Science Foundation and specifically the GEO Directorate through the Instrumentation and Facilities Program of the National Science Foundation under cooperative agreement EAR-1063471. The ETOPO1 and ETOPO2 bathymetry models are made available by the U.S. Department of Commerce, National Oceanic and Atmospheric Administration, and National Geophysical Data Center. We are grateful to Don Forsyth and Spahr Webb for the advice regarding DPG data analysis. We thank John Collins, Steve Ward, and three anonymous reviewers who provided comments that improved this paper. The OBS deployment was made possible with instruments and logistical support of the U.S. National Ocean Bottom Seismic Instrumentation Pool at Scripps Institute of Oceanography; in particular, thanks go to Jeff Babcock, Ernie Aaron, Phil Thai, and Mark Gibaud. The OBS deployment and recovery cruises were made possible with the equipment and logistical support of the University-National Oceanographic Laboratory System vessel fleet and staff support at Scripps with particular thanks to Jon Meyer, Brian Rowe, and Meghan Donohue. Kohler and Weeraratne thank Captain Curl and the crew of R/V *Melville* for their assistance during the 2010 OBS deployment cruise, and Captain Vullo and the crew of R/V New Horizon during the 2011 OBS recovery cruise. This work was supported by the National Science Foundation (grant OCE-0825254 and CyberSEES-1442665). Lin also acknowledges support for this research from the University of Utah.

References

Allgeyer, S., and P. Cummins (2014), Numerical tsunami simulation including elastic loading and seawater density stratification, *Geophys. Res. Lett.*, *41*, 2368–2375, doi:10.1002/2014GL059348.

Amante, C., and B. W. Eakins (2009), ETOPO1 1 arc-minute global relief model: procedures, data sources and analysis, *NOAA Technical Memorandum NESDIS NGDC-24,* 19 pp., March, 2009.

Bensen, G. D., M. H. Ritzwoller, M. P. Barmin, A. L. Levshin, F. Lin, M. P. Moschetti, N. M. Shapiro, and Y. Yang (2007), Processing seismic ambient noise data to obtain reliable broad-band surface wave dispersion measurements, *Geophys. J. Int.*, *169*, 1239–1260, doi:10.1111/j.165-246X.2007.03374.x.

Cox, C., T. Deaton, and S. Webb (1984), A deep-sea differential pressure gauge, *J. Atmos. Oceanic Technol.*, *1*, 246–237.

Gouédard, P., H. Yao, F. Ernst, and R. van der Hilst (2012), Surface wave eikonal tomography in heterogeneous media using exploration data, *Geophys. J. Int.*, *1*, 742.

Kohler, M. D., et al. (2010), ALBACORE OBS Deployment Cruise Report, 27 pp., R/V Melville Cruise MV1010. [Available at kohler.caltech.edu/Offshore/ALBACORE_2010_Cruise_Report.pdf, 14–27 August.]

Kohler, M. D., et al. (2011), ALBACORE OBS Recovery Cruise Report, 35 pp., R/V New Horizon Cruise NH1111. [Available at kohler.caltech.edu/Offshore/ALBACORE_2011_Cruise_Report.pdf, 7–16 September.]

Lamb, H. (1932), *Hydrodynamics*, 6th ed., Cambridge Univ. Press, Cambridge, U. K.

Landau, L. D., and E. M. Lifshitz (1989), *Fluid Mechanics*, 2nd ed., Pergamon Press, New York.

Lay, T., and T. C. Wallace (1995), *Modern Global Seismology*, Academic Press, San Diego, Calif.

Levshin, A. L., T. B. Yanovskaya, A. V. Lander, B. G. Bukchin, M. P. Barmin, L. I. Ratnikova, and E. N. Its (1989), *Seismic Surface Waves in a Laterally Inhomogeneous Earth*, edited by V. I. Keilis-Borok, Kluwer Acad., Norwell, Mass.

Lin, F., M. P. Moschetti, and M. H. Ritzwoller (2008), Surface wave tomography of the western United States from ambient seismic noise: Rayleigh and Love wave phase velocity maps, *Geophys. J. Int.*, doi:10.1111/j.1365-246X.2008.03720.x.

Lin, F.-C., and M. H. Ritzwoller (2011), Helmholtz surface wave tomography for isotropic and azimuthally anisotropic structure, *Geophys. J. Int.*, *186*, doi:10.1111/j.1365-246X.2011.05070.x.

Lin, F.-C., M. H. Ritzwoller, and R. Snieder (2009), Eikonal tomography: Surface wave tomography by phase front tracking across a regional broad-band seismic array, *Geophys. J. Int.*, *177*, 1091–1110, doi:10.1111/j.1365-246X.2009.04105.x.

Lin, F.-C., M. H. Ritzwoller, Y. Yang, M. P. Moschetti, and M. J. Fouch (2011), Complex and variable crustal and uppermost mantle seismic anisotropy in the western United States, *Nat. Geosci.*, *4*, 55–61, doi:10.1038/ngeo1036.

Lin, F.-C., D. Li, R. W. Clayton, and D. Hollis (2013), High-resolution 3D shallow crustal structure in Long Beach, California: Application of ambient noise tomography on a dense seismic array, *Geophysics*, *78*(4), Q45–Q56, doi:10.1190/geo2012-0453.1.

Lin, P. (2008), *Numerical Modeling of Water Waves*, Taylor and Francis, New York.

Liu, P. L.-F., S. B. Woo, and Y. S. Choas (1998), Computer programs for tsunami propagation and inundation, *Tech. Rep.*, Cornell Univ.

Mordret, A., N. M. Shapiro, S. Singh, P. Roux, J.-P. Montagner, and O. I. Barkved (2013), Azimuthal anisotropy at Valhall: The Helmholtz equation approach, *Geophys. Res. Lett.*, *40*, 2636–2641, doi:10.1002/grl.50447.

National Geophysical Data Center (2006), 2-minute Gridded Global Relief Data (ETOPO2) v2, National Geophysical Data Center, NOAA. doi:10.7289/V5J1012Q.

Shao, G., X. Li, C. Ji, and T. Maeda (2011), Focal mechanism and slip history of the 2011 Mw9.1 off the Pacific coast of Tohoku earthquake, constrained with teleseismic body and surface waves, *Earth Planets Space*, *63*, 559–564.

Shearer, P. (1999), *Introduction to Seismology*, Cambridge Univ. Press, Cambridge, U. K.

Smith, W. H. F., and P. Wessel (1990), Gridding with continuous curvature splines in tension, *Geophysics*, *55*, 293–305.

Stehly, L., M. Campillo, and N. M. Shapiro (2007), Traveltime measurements from noise correlation: Stability and detection of instrumental time-shifts, *Geophys. J. Int.*, *171*, 223–230, doi:10.1111/j.1365-246X.2007.03492.x.

Tsai, V. C., J.-P. Ampuero, H. Kanamori, and D. J. Stevenson (2013), Estimating the effect of Earth elasticity and variable water density on tsunami speeds, *Geophys. Res. Lett.*, *40*, 492–496, doi:10.1002/grl.50147.

Watada, S., S. Kusumoto, and K. Satake (2014), Traveltime delay and initial phase reversal of distant tsunamis coupled with the self-gravitating elastic Earth, *J. Geophys Res. Solid Earth*, *119*, 4287–4310, doi:10.1002/2013JB010841.

Wielandt, E. (1993), Propagation and structural interpretation of nonplane waves, *Geophys. J. Int.*, *113*, 45–53.